RESEARCH ARTICLE

National Science Open
5: 20250065, 2026
https://doi.org/10.1360/nso/20250065

Materials Science

Special Topic: Intelligent Materials and Devices

Ultrafast control of terahertz harmonic generation by optically modulating carrier dynamics in nonlinear metasurfaces

Zhehao Ye[2], Yongzheng Wen[1,*], Chen Wang[1], Yong Tan[1], Renfei Zhang[3], Fuli Zhang[2,*], Yuancheng Fan[2] & Ji Zhou[1,*]

[1]*State Key Laboratory of New Ceramic Materials, School of Materials Science and Engineering, Tsinghua University, Beijing 100084, China;*
[2]*MOE Key Laboratory of Material Physics and Chemistry under Extraordinary Conditions, School of Physical Science and Technology, Northwestern Polytechnical University, Xi'an 710129, China;*
[3]*Research Center for Metamaterials, Wuzhen Laboratory, Jiaxing 314500, China*

*Corresponding authors (emails: wenyzheng@tsinghua.edu.cn (Yongzheng Wen); fuli.zhang@nwpu.edu.cn (Fuli Zhang); zhouji@tsinghua.edu.cn (Ji Zhou))

Received 9 October 2025; Revised 25 November 2025; Accepted 1 December 2025; Published online 5 December 2025

Abstract: The development of terahertz (THz) sources with wide spectral coverage and dynamic control is critical for advancing high-speed communication, high-resolution imaging, and reconfigurable photonics. However, conventional nonlinear materials exhibit weak harmonic responses and limited tunability at room temperature. Here, we propose a nonlinear THz metasurface that simultaneously enables the generation and optical modulation of both second and third harmonics with ultrafast switching speeds. The metasurface locally enhances THz magnetic and electric fields, which drive photoinduced carriers into anharmonic oscillations and produce harmonic emissions. Owing to the rapid excitations of free carriers, we achieve the modulation of SHG and THG with switching times of 4.31 and 3.98 ps, respectively, and their extinction ratios exceed 1000. Moreover, tuning the optical pump fluence enables amplitude modulation of harmonic outputs by dynamically manipulating carrier density and mobility. This single-device approach demonstrates a unified platform for generating, enhancing, and dynamically controlling multiple THz harmonics, offering new opportunities for reconfigurable THz sources and adaptive nonlinear photonic devices.

Keywords: terahertz, nonlinear metasurface, harmonic generation, optical modulation, ultrafast control

INTRODUCTION

Over the past decade, terahertz (THz) technology has undergone rapid development, demonstrating remarkable application potential in numerous fields such as non-destructive detection [1,2], next-generation wireless communications [3,4], and intelligent sensing [5–10]. Central to these technologies is the development of compact, efficient, and tunable THz sources. In particular, the ability to generate and manipulate multiple harmonic frequencies within a single device enables versatile functionalities such as multi-band operation, frequency multiplexing, and waveform synthesis, which are critical for developing reconfigurable and broadband THz systems. For instance, achieving high-resolution radar imaging requires sources operating at higher frequencies, while high-speed THz wireless links demand sources with broad spectral cov-

© The Author(s) 2025. Published by Science Press and EDP Sciences. This is an Open Access article distributed under the terms of the Creative Commons Attribution License (https://creativecommons.org/licenses/by/4.0), which permits unrestricted use, distribution, and reproduction in any medium, provided the original work is properly cited.

erage and rapid modulation capability [11,12].

Harmonic generation is an effective way to extend the operating frequency bandwidth for radiation sources. While effective harmonic conversion can be achieved in the microwave and optical bands using nonlinear materials [13–17], the coexistence of electronic and photonic effects in the THz band makes it challenging to obtain significant harmonic conversion with conventional nonlinear materials. Pioneering studies have demonstrated THz harmonic generation in advanced material platforms. For example, graphene and topological insulators can produce odd-order THz harmonics under high-power THz pumping [18–20]. Symmetry-broken superconductors can achieve the generation of THz even-order harmonics at the cryogenic temperatures [21]. However, these platforms suffer from complex fabrication, limited designability, or non-ambient operating conditions, hindering their integration into practical devices. Moreover, their harmonic responses are often fixed by intrinsic properties, making dynamic modulations extremely challenging to achieve.

Metamaterials, composed of subwavelength artificial unit cells, enable unprecedented manipulations of electromagnetic properties beyond natural materials. Their two-dimensional counterpart, metasurfaces, has facilitated a wide range of low-loss, easily integrated functional devices [22–30]. By relaxing phase-matching constraints, enabling monolithic integration, and offering tunable bandwidth, metasurfaces provide a promising platform for nonlinear optics across microwave [31,32], visible [33,34], and infrared frequencies [35]. Introducing active control further expands functionality. Compared with electrical, thermal, or mechanical tuning, optical pumping affords non-contact, spatially selective, and ultrafast modulation [36,37]. Previous studies on reconfigurable THz metasurfaces have demonstrated that optical pumping enables high-speed and efficient control of linear responses [38,39]. More recently, leveraging the strategically designed field coupling and enhancements in the semiconductor-based metasurfaces, the efficient second and third harmonic generation (SHG and THG) at the THz frequencies has been realized at room temperature [40–42]. Despite these advances, simultaneous generation and ultrafast modulation of multiple THz harmonics within a single metasurface remains an open challenge. The synergistic combination of metasurface-induced field enhancement and optical control of carrier dynamics offers a powerful strategy for realizing dynamic, room-temperature THz nonlinear sources. It becomes possible to design functional metasurfaces capable of generating, controlling, and switching multi-order harmonic radiation on picosecond timescales, paving the way for adaptive THz photonic systems and high-speed signal processing.

In this work, we propose and experimentally demonstrate a nonlinear THz metasurface capable of simultaneously generating and ultrafast optically modulating second and third harmonics at room temperature. The metasurface, composed of gold split-ring resonators (SRRs) on a semiconductor substrate, leverages strong local electromagnetic field enhancement to drive the anharmonic motion of photoinduced carriers, resulting in efficient SHG and THG. Optical pumping dynamically tailors the carrier density and mobility, allowing precise control of harmonic amplitude and temporal response, with picosecond-level switching times and very high extinction ratios. This work establishes a unified platform for generating, enhancing, and dynamically tuning THz nonlinear processes, offering a promising route toward reconfigurable THz sources and adaptive nonlinear photonic systems.

RESULTS

Figure 1a illustrates the concept of the proposed nonlinear THz metasurface that enables optically tunable

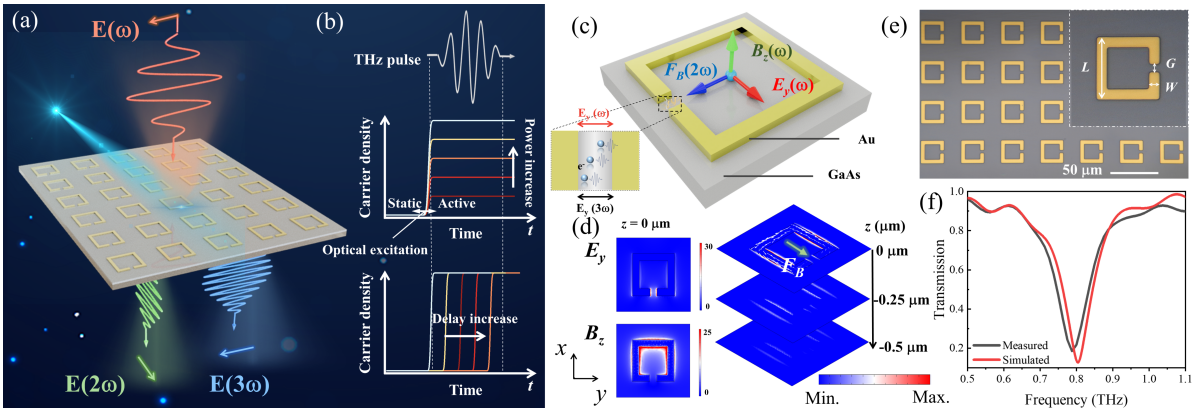

Figure 1 Principle of the THz nonlinear metasurface and resonance characterization. (a) Schematic of the designed metasurface. (b) Schematic of dynamically controlling carrier dynamics during a terahertz pulse by tuning optical pump fluence and time delay. The optical excitation defines the transition from the static to the active state. (c) Illustration of orientations of the local electric field $E_y(\omega)$, magnetic field $B_z(\omega)$, the Lorentz force $F_B(2\omega)$, and the carrier drift in the pumped GaAs driven by the local electromagnetic field. (d) The current disturbance (white arrow), the local enhancement of magnetic field in the z-axis $B_z(\omega)$, the local enhancement of electric field in the y-axis ($E_y(\omega)$), and the normalized distribution of the Lorentz force $F_B(2\omega)$. (e) Photomicrograph of the fabricated metasurface, where the insert shows the unit cell of the metasurface: W = 4 μm, G = 4 μm, L = 24 μm, and the period of the unit cell is 42 μm. (f) Simulated and measured transmission spectrum of the metasurface.

harmonic generation. The device consists of a periodic array of gold SRRs patterned on an intrinsic GaAs substrate. The choice of GaAs is motivated by its direct bandgap and superior carrier mobility, which are crucial for efficient optical modulation and ultrafast switching at the pump wavelength. In the static state, without optical excitation, neither gold nor intrinsic GaAs exhibits significant THz nonlinear responses, regardless of resonance, and the metasurface is not expected to generate SHG or THG. Once illuminated by the optical excitation whose photon energy exceeds the bandgap of intrinsic GaAs, free carriers are generated quasi-instantaneously [43], transforming the metasurface into an active state, as shown in Figure 1b. This process establishes the foundation for optical modulation of carrier dynamics, as the density and mobility of carriers can be precisely controlled through the optical pump fluence and delay, thereby tuning the nonlinear response on a picosecond timescale.

Specifically, the underlying mechanisms of SHG and THG are shown schematically in Figure 1c. When the incident THz field drives the SRRs at the inductive-capacitive (LC) resonance, a strong local dynamic magnetic field along the z-axis ($B_z(\omega)$) and electric field along the y-axis ($E_y(\omega)$) are produced, as shown in Figure 1d. The photoinduced carriers in the pumped GaAs, positioned within the enhanced electromagnetic field of the SRRs, are driven by the local electric field to move along the y direction with a drift velocity v_y, oscillating with frequency ω. Simultaneously, the magnetic field component $B_z(\omega)$ exerts a Lorentz force $F_B = qv_y \times B_z$ on the photoinduced carriers with a frequency-doubled component perpendicular to both $B_z(\omega)$ and $E_y(\omega)$ [44]. This magnetoelectric coupling induces an anharmonic carrier motion along the cross-polarization (x-axis) with doubled frequency 2ω, thereby generating second harmonic radiation.

Simultaneously, the THG originates from the intrinsic third-order nonlinearity of the photoexcited GaAs [45]. Within the SRR gap, the strongly enhanced local electric field induces nonlinear carrier transport, governed by field-dependent mobility and scattering rates, which collectively give rise to a macroscopic nonlinear current density coupled to the local field through a cubic dependence [45,46]. Given the effective isotropy of the GaAs substrate and the designed SRR structure, ensuring the local driving field polarization

remains parallel to the incident THz field, the resulting THz THG maintains a co-polarized (*y*-axis) state relative to the fundamental excitation. Thus, the polarization distinction between SHG and THG stems from their fundamentally different microscopic origins. The former from Lorentz-force-induced cross-axis motion, and the latter from field-driven nonlinear transport along the primary polarization (details of the theoretical models and simulated results are provided in Sections S1 and S2 of the Supplementary information).

Because both processes rely on the transient behavior of photoinduced carriers, the nonlinear emission can be dynamically tuned through the optical excitation. The amplitude of this nonlinear response is intrinsically governed by material parameters, including the carrier concentration, carrier mobility, and local field enhancement within the SRR [40,47]. Varying the optical pump fluence modulates the carrier density and mobility, whereas adjusting the pump-THz delay controls their temporal evolution. These factors collectively determine the harmonic emission strength, forming the physical foundation for the ultrafast optical modulation demonstrated below. To verify this mechanism, we fabricated a proof-of-principle metasurface with the fundamental frequency of 0.8 THz, shown in Figure 1e. The resonance characteristic of the metamaterial sample is shown in Figure 1f (details of linear spectra measurement are provided in Section Experimental setups). A pronounced transmission dip observed at 0.8 THz confirms the resonant frequency, consistent with simulated predictions. The slight discrepancy between the simulated and measured results can be attributed to machining inaccuracies in the fabricated samples.

Ultrafast control of SHG and THG was experimentally demonstrated using a time-resolved optical pump-THz probe system with the femtosecond optical excitation at the wavelength of 800 nm. The incident THz pulse, centered at 0.8 THz with a peak field of 20 kV/cm, excites the metasurface (details of the experimental setup can be seen in Section S3). According to the theoretical model, SHG is expected to occur in a cross-polarized state relative to the fundamental excitation. We therefore first examined the normalized cross-polarized signals from the metasurface, as shown in Figure 2a. The gray line and red line denote the signals without and with 800 nm wavelength optical pumping, respectively. Without optical pumping, the cross-polarization component is observed only at the 0.8 THz fundamental frequency, indicating the lack of intrinsic SHG in the sample under a strong THz field. When optical pumping is applied, a characteristic peak appears in the cross-polarized spectral component centered at 1.6 THz, indicating the generation of the second harmonic. The inset shows the signal of SHG in the time domain. The experimental results demonstrate that the free charge carriers generated by optical pumping can be effectively driven by local electromagnetic fields to emit THz harmonic radiation.

Due to the much longer duration of the THz pulse compared with the femtosecond optical pulse, the timing of photoinduced carrier generation can be precisely controlled by adjusting the relative time delay between the two pulses as they reach the metasurface. This enables ultrafast modulation of the harmonic radiation through the temporal dynamics of the carriers. The relative time delay is defined as $t_{\mathrm{delay}} = t_{800\mathrm{nm}} - t_{\mathrm{THz}}$, where $t_{800\mathrm{nm}}$ and t_{THz} are the arrival times of the optical pump and the THz pulse at the metasurface, respectively. In the experiment, the t_{delay} is controlled by adjusting $t_{800\ \mathrm{nm}}$ while keeping t_{THz} fixed. The experimental results of the ultrafast modulation dynamic behavior of the SHG are shown in Figure 2b. The results demonstrate that when $t_{\mathrm{delay}} < 1.7$ ps, the device remains in its "OFF" state with no measurable SHG, equivalent to the situation without optical pumping. As the time delay t_{delay} further increases, the SHG

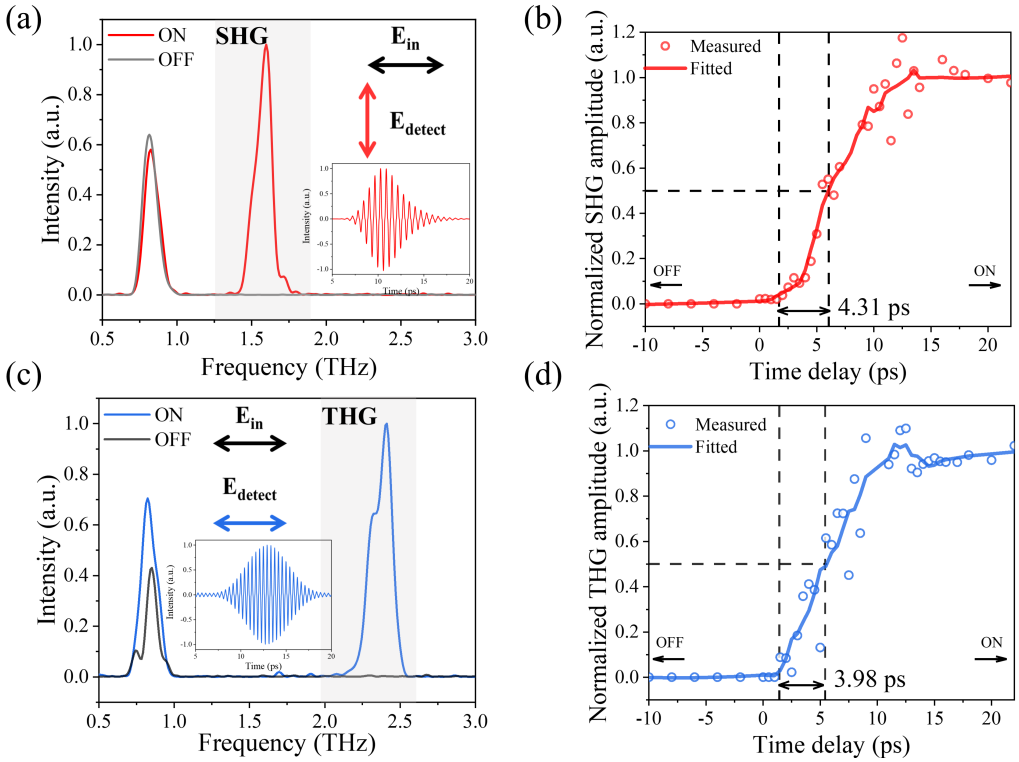

Figure 2 Ultrafast switching of SHG and THG. (a) Normalized cross-polarized signals with and without optical pumping; the inset shows the corresponding time-domain second harmonic signal. (b) Normalized SHG amplitude versus the relative time delay of the optical pump and fundamental THz pulse. (c) Normalized co-polarized signals with and without optical pumping; the inset shows the corresponding time-domain third harmonic signal. (d) Normalized THG amplitude versus the relative time delay of the optical pump and fundamental THz pulse.

amplitude gradually rises from zero to its maximum value. This behavior occurs because the optical pump initiates free carrier generation just before the trailing edge of the strong THz pulse arrives. These photo-induced carriers are then accelerated by the remaining high-field portion of the THz pulse, resulting in stronger SHG. Beyond the maximum, further increasing the time delay t_{delay} results in the metasurface exhibiting approximately stable SHG radiation. This steady-state emission occurs because the optical pump pulse precedes the entire THz pulse, enabling the generation of a large, stable population of photoinduced carriers in the GaAs substrate before the THz field arrives. Analysis of the harmonic response as a function of time delay, the extracted switching time is 4.31 ps, which is several orders of magnitude faster than thermal relaxation, confirming the non-thermal origin of the modulation [48], and the extinction ratio exceeds 1416, demonstrating picosecond-scale control of nonlinear conversion.

For the THG from the metasurface, the normalized signal measured under co-polarization is shown in Figure 2c. The black line represents the co-polarized signal without optical pumping, while the blue line represents the co-polarized signal with optical pumping. In the absence of optical pumping, similar to the SHG, there is only a fundamental frequency characteristic peak in the frequency spectrum. There is a small dip near 0.8 THz due to the resonance of the metasurface, which is manifested in co-polarization detection. When there is optical pumping, a third harmonic signal peak appears in the spectrum of the co-polarization, originating from the anharmonic carrier oscillations of photoinduced carriers driven by the intense THz electric field. At this point, the small dip of its fundamental frequency disappears due to the introduction of

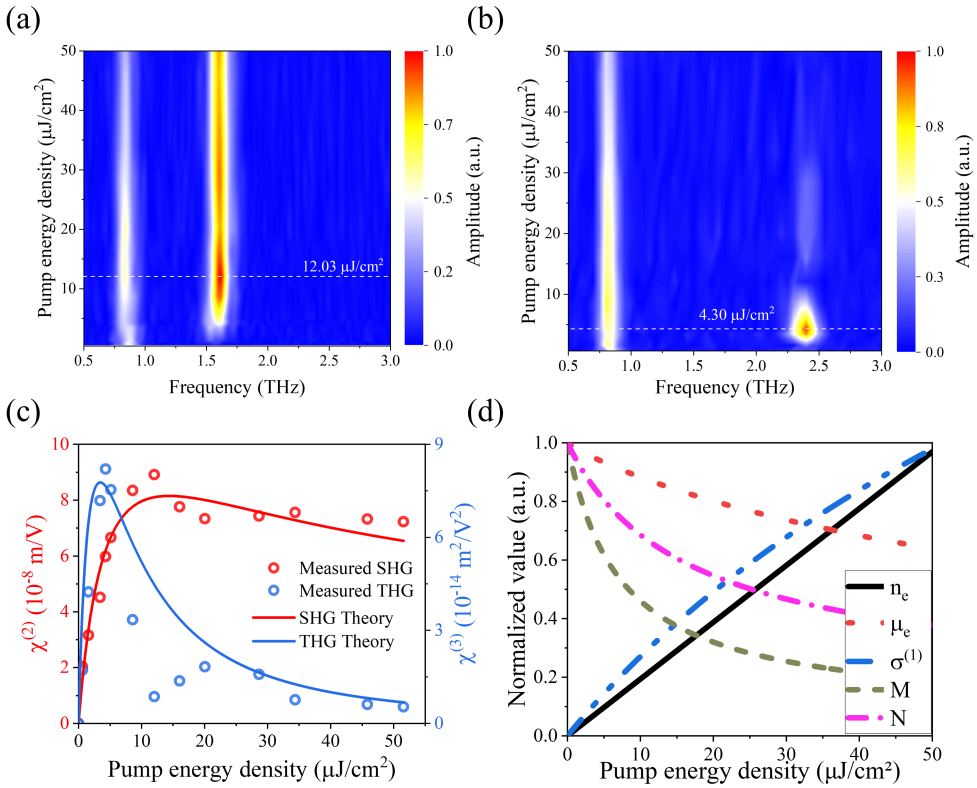

Figure 3 Modulation of the amplitude of SHG and THG. (a) Normalized measured THz SHG amplitude as a function of the optical pump energy density. (b) Normalized measured THz THG amplitude as a function of the optical pump energy density. (c) Measured and theoretical results of the $\chi^{(2)}$ and $\chi^{(3)}$ as a function of the different optical pump energy density. (d) The normalized value of the carrier concentration n_e, mobility μ_e, linear conductivity $\sigma^{(1)}$, the local enhancement factors of the electric (M) and magnetic (N) fields, corresponding to the pump energy density.

charge carriers, which increases the conductivity and degrades the resonance characteristics of the metasurface [49,50]. The ultrafast modulation of the THG is shown in Figure 2d. Owing to the dependence of its signal strength on the THz pulse duration interacting with photoinduced carriers, the THG shows similar ultrafast modulation characteristics of SHG, including a switching speed of approximately 3.98 ps. The device also exhibits a clear switching behavior for THG. The normalized harmonic intensity is ~0 in the "OFF" state, resulting in a high extinction ratio of approximately 1285 for THG.

We note that the modulation speeds for both SHG and THG are primarily governed by the carrier density rather than the thermal or structural effects. The metasurface enables ultrafast, non-contact control of nonlinear emission at room temperature. These findings confirm that optical excitation acts as an effective "gate" for dynamically tuning the nonlinear THz emission through real-time manipulation of carrier dynamics.

We further demonstrate dynamic control of both SHG and THG intensities by modulating the optical-pump intensity to vary the density of the photoinduced carriers. To ensure the optical pump arrives earlier than the entire THz pulse, the device is maintained in its fully "ON" state during testing. The dynamic regulation of the harmonic via optical pump intensity is shown in Figure 3a and b, respectively. The SHG and THG intensities exhibit distinctly different dependencies on the optical pumping energy density. For the SHG

signal shown in Figure 3a, as the energy density of the optical pump increases, its signal strength briefly rises and reaches its maximum value at 12.03 μJ/cm^2, and then decreases gradually. As shown in Figure 3b, the THG signal amplitude rises sharply and reaches its maximum at a lower energy density of 4.30 μJ/cm^2. However, beyond this threshold, it decreases sharply with increasing optical pump energy. The distinct evolution behaviors of SHG and THG in the metasurface can be attributed to the dynamic process of carrier density and its related parameters (mobility and local THz field strength) under different optical pumping energy densities. Increasing optical energy density increases the carrier density, but it also increases the linear conductivity, leading to resonance damping and field screening that reduce local field strength. In parallel, enhanced carrier-carrier and carrier-phonon scattering can reduce mobility. The competition among these effects results in an optimal energy density for each nonlinear process.

According to the definition of the second-order nonlinear susceptibility $\chi^{(2)}$ is given by the modified Drude model (the details are provided in Sections S1 and S4). Due to the definition of $I_{2\omega} = \left|\varepsilon_0 \cdot \chi^{(2)} E_{\mathrm{loc}} \cdot E_{\mathrm{loc}}\right|^2$, the SHG intensity is derived to scale as

$$I_{2\omega} \propto \left(\langle n_e \rangle \cdot \langle \mu_e \rangle\right)^2 (M \cdot N)^2 \propto \left(\sigma^{(1)} \cdot M \cdot N\right)^2, \tag{1}$$

where $\langle n_e \rangle$, $\langle \mu_e \rangle$, and $\sigma^{(1)}$ are the average carrier concentration, the average carrier mobility, and the linear conductivity of the pumped GaAs, respectively. The Eq. (1) demonstrates that the SHG intensity scales quadratically with the product of the linear conductivity $\sigma^{(1)}$, the local enhancement factors of the electric (M) and magnetic (N) fields. It should be noted that the carrier concentration is a function of the optical pumping energy density and increases with it, while the carrier mobility $\langle \mu_e \rangle$ decreases as the carrier concentration $\langle n_e \rangle$ rises [51]. Linear conductivity is the product of the carrier concentration and mobility.

For THG, the third-order nonlinear susceptibility $\chi^{(3)}$ can be derived from a simplified Boltzmann transport equation (the details are provided in Sections S1 and S4) [52,53]. According to the definition $I_{3\omega} = \left|\varepsilon_0 \cdot \chi^{(3)} E_{\mathrm{loc}} \cdot E_{\mathrm{loc}} \cdot E_{\mathrm{loc}}\right|^2$, the THG intensity exhibits a dependence as

$$I_{3\omega} \propto (\langle n_e \rangle^2 \cdot \langle \mu_e \rangle^6) M^6 \propto (\sigma^{(1)})^2 \langle \mu_e \rangle^4 M^6. \tag{2}$$

Eq. (2) suggests that the intensity of the THG is related to the square of linear conductivity $\sigma^{(1)}$, the fourth power of carrier mobility $\langle \mu_e \rangle$, and the sixth power of local electric field enhancement factor M. This indicates that the THG intensity is more sensitive to the decrease in carrier mobility caused by the increase of optical pump energy density compared with the SHG intensity. Specifically, as the linear conductivity increases, the local field enhancement effect weakens (the detail is provided in Section S4). Figure 3c delineates the experimentally measured $\chi^{(2)}$ and $\chi^{(3)}$, as a function of the applied optical pump energy density (details are provided in Section S5). Within the optical pump range from 0.63 to 51.58 μJ/cm^2, the effective $\chi^{(2)}$ can be dynamically adjusted across the range from 2.1 × 10^{-8} to 9.1 × 10^{-8} m/V, while the effective $\chi^{(3)}$ varies from 7 × 10^{-15} to 8.2 × 10^{-14} m^2/V^2. To clarify the dynamic behavior of the photoinduced carriers under varying optical pump energy densities, we perform theoretical fitting on the normalized SHG and THG intensities based on the established model. The resulting theoretical effective second- and third-order susceptibility variations are plotted alongside the experimental data in Figure 3c. The theoretical model predicts the dependence of effective $\chi^{(2)}$ and $\chi^{(3)}$ on the optical pump energy density, respectively. Crucially, this

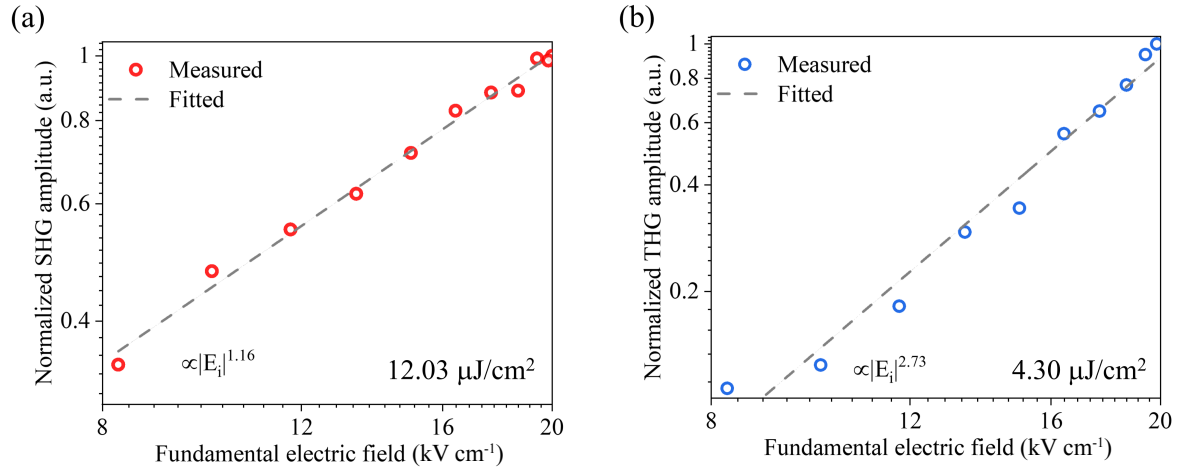

Figure 4 Dependence of normalized field intensity of the metasurface on the fundamental electric field, including the field strength of SHG (a) and THG (b).

tunability enables the precise dynamic control over the normalized intensity ratio between the second and third harmonics, which establishes a strong foundation for realizing high-speed communication applications.

The phenomena can be explained theoretically by the interplay between these competing and synergistic factors of carrier density, carrier mobility, and the field enhancement effect in Figure 3d. The linear conductivity (the product of carrier density and mobility) increases across the tested range of pump energy density. Within this range, the resulting high conductivity of GaAs significantly weakens the field enhancement properties originally induced by the SRRs [54,55]. With rising pump energy density, the carrier concentration increases rapidly, accompanied by a significant enhancement in linear conductivity and a concurrent reduction in carrier mobility, magnetic field enhancement factor, and electric field enhancement factor. Particularly, since the THG exhibits a stronger dependence on the field enhancement factor and carrier mobility than the SHG, its optimal pump energy density is lower than that of the SHG.

As the optical pump energy density continues to increase beyond the optimal point, the generation of additional photoinduced carriers leads to a further reduction in carrier mobility. The decrease in carrier mobility and the decline in the field enhancement factor become the dominant factor. The effective $\chi^{(3)}$ is especially more sensitive to the reduction in both carrier mobility and the field enhancement factor compared to the effective $\chi^{(2)}$. Consequently, beyond the optimal pump energy density, the THG intensity decreases rapidly with further increases in pump energy, whereas the SHG intensity shows a more gradual decrease. Together, these findings confirm that optical-pump fluence provides an effective means for broadband amplitude modulation of THz nonlinear processes by precisely controlling carrier concentration and mobility.

The measured pump-power dependence of the SHG and THG at optimal pumping is presented in Figure 4a and b, respectively. The SHG and THG intensities follow power-law dependencies with exponents of 1.16 and 2.73, respectively, deviating significantly from the conventional quadratic and cubic relationships. The observed phenomenon is attributable to the intervalley scattering effect. In this experiment, the optical pump with photon energy of 1.55 eV is utilized, lying between the Γ-valley bandgap (~1.42 eV) and the L-valley

bandgap (~1.71 eV) of the GaAs. Consequently, the pump light selectively excites electrons from the valence band to the Γ-valley of the conduction band, yet lacks sufficient energy to directly excite them into the higher-energy L-valley. Under the local enhancement of the electromagnetic field, these free electrons are driven by the strong THz field, acquiring large ponderomotive energy. This strong driving force scatters electrons from the Γ-valley into the L-valley, thereby initiating the intervalley scattering process. The effective masses of electrons in the Γ and L valleys are $0.067m_0$ and $0.55m_0$, respectively (m_0 is the free electron mass). The larger effective mass in L-valley decreases the effective carrier mobility. This scattering event increases the effective mass of the carriers and significantly decreases their mobility, leading to a measurable reduction of nonlinear susceptibility [56]. This combined effect thereby causes the observed deviations from the ideal quadratic and cubic power dependencies, resulting in a measurable reduction in the conversion efficiency of both SHG and THG (see Section S6 for details).

We have developed a metasurface device that utilizes carrier dynamics modulation to simultaneously generate, enhance, and dynamically control THz nonlinear harmonics. The proposed mechanism for both harmonic generation and modulation exhibits broad applicability across a wide frequency range, enabling its extension to metasurfaces operating in other frequency bands and to devices responsive to alternative external stimuli. Furthermore, by precisely engineering the metasurface unit-cell structures or by introducing complex localized field distributions arising from multiple resonant modes, flexible control over key characteristics of the harmonic radiation, such as operating frequency, phase, polarization, and even higher-order harmonic generation, can be achieved [57–60]. The proposed mechanism, based on the ultrafast modulation of carrier dynamics, offering an ideal method for exploring and realizing reconfigurable THz nonlinear effects, can be readily extended to various semiconductor material platforms with suitable band gaps. Although the 800 nm excitation used in this work is optimized for GaAs, the same principle can be applied to other semiconductors. For example, excitation at 1.03 or 1.55 μm would be suitable for narrower-bandgap materials such as InAs or Ge, enabling flexible adaptation of the approach across different spectral ranges. These advantages are expected to significantly advance the development and practical application of high-performance THz radiation sources and integrated functional devices.

CONCLUSIONS

In summary, we have theoretically and experimentally demonstrated an ultrafast optically reconfigurable nonlinear metasurface that realizes efficient SHG and THG in the THz regime at room temperature. The nonlinear emission originates from anharmonic carrier dynamics induced by strongly enhanced local magnetic and electric fields within the metasurface, while the optical modulation provides direct control over carrier density and mobility, enabling dynamic tuning of both harmonic amplitude and switching state. The metasurface exhibits picosecond-scale response times (4.31 ps for SHG and 3.98 ps for THG) with extinction ratios exceeding 1000, and supports broad amplitude modulation via optical pump fluence. These findings provide a general and unified strategy for realizing ultrafast, tunable nonlinear responses in semiconductor-based metasurfaces, offering potential for reconfigurable THz photonic devices and THz sources. Furthermore, the underlying concept of optically controlled carrier dynamics is not limited to the THz band and could be extended to other frequency ranges, such as the mid-infrared, with appropriate design of the

metasurface geometry and semiconductor properties.

MATERIALS AND METHODS

Sample fabrication

The metasurface was fabricated on high-resistivity (>100 kΩ cm) (001) GaAs substrates (625 μm thickness, dual-side-polished). Metasurface patterns were lithographically defined using ultraviolet (UV) photolithography. Subsequent electron-beam deposition of Ti/Au (30 nm/200 nm) bilayers was performed, with final structures released by solvent-assisted lift-off in acetone.

Experimental setups

Linear spectra measurement

A Ti:sapphire femtosecond laser system (central wavelength: 800 nm, repetition rate: 1 kHz, pulse energy: 7 mJ) was divided into two beams using a beam splitter. One beam served as the probe, and its energy was attenuated to below 1 μJ using a variable neutral density filter before entering the electro-optic detection arm, ensuring operation in the linear response regime. The other pumped a commercial optical parametric amplifier (OPA) to generate 1550 nm wavelength pulses. A broadband THz pulse was produced by irradiating an organic nonlinear crystal, 2-(3-(4-hydroxystyryl)-5,5-dimethylcyclohex-2-enylidene) malononitrile (OH1), with the 1550 nm wavelength femtosecond laser. To ensure measurements in the linear transmission regime, the 1550 nm wavelength laser pulse energy was attenuated to approximately 0.15% of its original intensity using calibrated optical attenuators before excitation of the OH1 crystal. The generated THz beam was focused by off-axis parabolic mirrors onto the sample and detected using a standard electro-optic sampling (EOS) setup with a 1.0 mm-thick ZnTe crystal. All experiments were performed at room temperature under a dry N_2 purge with a relative humidity of < 5%. The transmitted THz time-domain waveforms of the metasurface sample and a bare GaAs substrate were recorded, and their Fourier-transformed spectra were divided to obtain the electric field amplitude transmission spectrum.

Nonlinear spectra measurement

The same femtosecond laser from the Ti:sapphire femtosecond laser system was divided into three beams. One beam served as the probe, attenuated to below 1 μJ using a variable neutral density filter before entering the electro-optic detection arm, ensuring operation in the linear response regime. Another pumped an OPA to generate 1550 nm wavelength pulses, and the third provided 800 nm wavelength excitation for photoinduced carrier generation in the GaAs substrate. A broadband THz pulse was produced by irradiating an organic nonlinear crystal, OH1, with the 1550 nm wavelength femtosecond laser. The generated THz beam passed through a bandpass filter centered at 0.8 THz to suppress residual high-frequency background, followed by two wire-grid polarizers for fundamental-wave calibration. The THz beam was then focused by off-axis parabolic mirrors onto the sample. The 800 nm wavelength pump beam was focused to a spot size of approximately 2 mm in diameter, which was significantly larger than the 1 mm diameter spot of the focused

THz beam.

The optical pump intensity and relative time delay were independently tuned using neutral-density filters and a mechanical delay line, achieving a temporal resolution of ~0.2 ps. To isolate the nonlinear response, bandpass filters transmitting SHG or THG while suppressing the fundamental field were placed after the sample. The harmonic signals were detected using a standard EOS setup with a 1.0 mm-thick ZnTe crystal. By rotating the ZnTe [001] axis, both co- and cross-polarization harmonic electric-field amplitudes were sequentially recorded. The estimated steady-state temperature rise of the sample under our experimental conditions (< 60 μJ cm^{-2} pump fluence, 1 kHz repetition rate) was 0.24 K, according to standard heat diffusion models (details are provided in Section S7). Therefore, thermal accumulation can be safely neglected. All measurements were conducted at room temperature under a dry N_2 atmosphere with a relative humidity of < 5% (details are provided in Section S3).

Simulation setting

Details of the simulation setup are provided in the Supplementary information. The linear transmission spectrum of the metasurface was modeled using the finite-difference time-domain (FDTD) method. The high-resistivity GaAs substrate was treated as semi-infinite (ε_{GaAs} = 12.9), and the 200 nm gold layer was modeled as a lossy metal with a conductivity of 4.1×10^7 S/m. A single unit cell was simulated in the time domain with periodic boundary conditions along the *x* and *y* directions and open boundaries along the propagation (*z*) axis. A broadband *y*-polarized (perpendicular to the SRR gap) plane wave served as the excitation source. The *y*-component of the transmitted electric field was recorded at the exit plane of the GaAs substrate. A Hanning window was applied to the time-domain signal to suppress Fabry-Perot reflections from the substrate interfaces. The linear transmission spectra can be derived through the Fourier transformation of time-domain signals:

$$T(\omega) = \left| \frac{\mathcal{F}\{E_{\text{sample}}(t)\}}{\mathcal{F}\{E_{\text{reference}}(t)\}} \right|, \tag{3}$$

where $T(\omega)$ denotes frequency-dependent transmittance normalized to the reference structure. $E_{\text{sample}}(t)$ and $E_{\text{reference}}(t)$ are the signals in the time domain of the metasurface and GaAs substrate, respectively.

The nonlinear response of the metasurface was simulated in the time domain by the commercial software COMSOL Multiphysics, based on the finite element method (FEM) using a linearly polarized Gaussian pulse plane wave incident from the top, with *y*-polarization.

For the second harmonic generation, the magnetoelectric coupling effect in the pumped metasurface can be described as an anisotropic conductivity tensor:

$$\tilde{\sigma}(B,\omega) = \tilde{\sigma}_0(\omega) \begin{pmatrix} \frac{1}{1+\beta^2} & -\frac{\beta}{1+\beta^2} & 0 \\ \frac{\beta}{1+\beta^2} & \frac{1}{1+\beta^2} & 0 \\ 0 & 0 & 1 \end{pmatrix}, \tag{4}$$

where $\beta(\omega) = \mu_e(\omega)\mathbf{B}_z(\omega)$, $\mathbf{B}_z(\omega)$ denotes the local magnetic field amplitude along the *z*-axis, $\tilde{\sigma}_0(\omega)$ and

$\mu_e(\omega)$ denote the conductivity and at the fundamental angular frequency ω, respectively.

For the third harmonic generation, the third-order nonlinearity response of the pumped GaAs layer was defined as follows:

$$P_{3\omega} = \varepsilon_0 \chi^{(3)} E_y^3, \tag{5}$$

where ε_0 is the permittivity of free space, $\chi^{(3)}$ is the third-order nonlinear susceptibility, and E_y is the localized electric field amplitude along the y-axis.

Data availability

The original data are available from the corresponding authors upon reasonable request.

Funding

This work was supported by the National Key R&D Program of China (2023YFB3811400), the Basic Science Center Project of the National Natural Science Foundation of China (52388201), the National Natural Science Foundation of China (52332006, 12504387), the Beijing Natural Science Foundation (Z240008), and the China Postdoctoral Science Foundation (BX20250299, 2025M773396).

Author contributions

Z.Y. conducted the investigation, designed the methodology, performed the experiments, curated the data, and wrote and revised the manuscript; C.W. acquired funding and reviewed and edited the manuscript; Y.T. and R.Z. performed the experiments; Y.F. acquired funding; Y.W., F.Z. and J.Z. acquired funding and administered the project; Y.W. conceived the idea, supervised the research, provided resources, and reviewed and edited the manuscript. The manuscript reflects the contributions of all authors.

Conflict of interest

The authors declare no conflict of interest.

Supplementary information

The supporting information is available online at https://doi.org/10.1360/nso/20250065. The supporting materials are published as submitted, without typesetting or editing. The responsibility for scientific accuracy and content remains entirely with the authors.

References

1 Wang K, Sun DW, Pu H. Emerging non-destructive terahertz spectroscopic imaging technique: Principle and applications in the agri-food industry. *Trends Food Sci Tech* 2017; **67**: 93–105.

2 Uzundal CB, Feng Q, Tang W, *et al.* Efficient on-chip terahertz generation and detection with GaN photoconductive emitters. *Light Sci Appl* 2025; **14**: 226.

3 Shen D, Lan F, Wang L, *et al.* Sub-terahertz transmissive reconfigurable intelligent surface for integrated beam steering and self-OOK-modulation. *Light Sci Appl* 2025; **14**: 13.

4 Kim H, Kang C, Jang D, *et al.* Ionizing terahertz waves with 260 MV/cm from scalable optical rectification. *Light Sci Appl* 2024; **13**: 118.

5 Chen B, Wang X, Li W, *et al.* Electrically addressable integrated intelligent terahertz metasurface. *Sci Adv* 2022; **8**: eadd1296.

6 Xi T, Jiang H, Li J, *et al.* Terahertz sensing based on the nonlinear electrodynamics of the two-dimensional correlated topological semimetal $TaIrTe_4$. *Nat Electron* 2025; **8**: 578–586.

7 Hou Z, Chen L, Gao X, *et al.* High-sensitivity integrated terahertz sensor with large dynamic range based on adjustable high-Q microring resonator. *APL Photon* 2024; **9**: 126109.

8 Wang R, Hao R, Li D, *et al.* Multifunctional terahertz biodetection enabled by resonant metasurfaces. *Adv Mater* 2025; **37**: 2418147.

9 El-Helou AJ, Liu Y, Chen C, *et al.* Optical metasurfaces for the next-generation biosensing and bioimaging. *Laser Photon Rev* 2025; **19**: 2401715.

10 Beruete M, Jáuregui-López I. Terahertz sensing based on metasurfaces. *Adv Opt Mater* 2020; **8**: 1900721.

11 Liu K, Feng Y, Han C, *et al.* High-speed 0.22 THz communication system with 84 Gbps for real-time uncompressed 8K video transmission of live events. *Nat Commun* 2024; **15**: 8037.

12 Li X, Li J, Li Y, *et al.* High-throughput terahertz imaging: Progress and challenges. *Light Sci Appl* 2023; **12**: 233.

13 Schied E, Weis O. Microwave-harmonic generation in ferrites at high power. *J Magn Magn Mater* 1984; **45**: 377–381.

14 Persico F, Vetri G. Theory of second-harmonic generation at microwave frequencies by paramagnetic materials. *Phys Rev B* 1973; **8**: 3512–3536.

15 Wang ZY, Wu X, Xiong X, *et al.* Toward ultimate-efficiency frequency conversion in nonlinear optical microresonators. *Sci Adv* 2025; **11**: eadu7605.

16 Fan Q, Ma Y, Xu H, *et al.* Near-room-temperature reversible switching of quadratic optical nonlinearities in a one-dimensional perovskite-like hybrid. *Microstructures* 2022; **2**: 13.

17 Zhang J, Neufeld O, Tancogne-Dejean N, *et al.* Enhanced high harmonic efficiency through phonon-assisted photodoping effect. *npj Comput Mater* 2024; **10**: 202.

18 Hafez HA, Kovalev S, Deinert JC, *et al.* Extremely efficient terahertz high-harmonic generation in graphene by hot Dirac fermions. *Nature* 2018; **561**: 507–511.

19 Bowlan P, Martinez-Moreno E, Reimann K, *et al.* Ultrafast terahertz response of multilayer graphene in the nonperturbative regime. *Phys Rev B* 2014; **89**: 041408.

20 Giorgianni F, Chiadroni E, Rovere A, *et al.* Strong nonlinear terahertz response induced by Dirac surface states in Bi_2Se_3 topological insulator. *Nat Commun* 2016; **7**: 11421.

21 Cheng B, Kanda N, Ikeda TN, *et al.* Efficient terahertz harmonic generation with coherent acceleration of electrons in the Dirac semimetal Cd_3As_2. *Phys Rev Lett* 2020; **124**: 117402.

22 Nayani PS, Moradi M, Salami P, *et al.* Passive highly dispersive matching network enabling broadband electromagnetic absorption. *Nat Commun* 2025; **16**: 905.

23 Zheludev NI, Kivshar YS. From metamaterials to metadevices. *Nat Mater* 2012; **11**: 917–924.

24 Wang S, Wu PC, Su VC, *et al.* A broadband achromatic metalens in the visible. *Nat Nanotech* 2018; **13**: 227–232.

25 Chen X, Luo W, Zhao R, *et al.* Ceramic-based meta-material absorber with high-temperature stability. *Rare Met* 2024; **43**: 4433–4440.

26 Zhou C, Huang L, Jin R, *et al.* Bound states in the continuum in asymmetric dielectric metasurfaces. *Laser Photon Rev* 2023; **17**: 2200564.

27 Genevet P, Capasso F, Aieta F, *et al.* Recent advances in planar optics: From plasmonic to dielectric metasurfaces. *Optica* 2017; **4**: 139.

28 Zhang M, Pu M, Zhang F, *et al.* Plasmonic metasurfaces for switchable photonic spin-orbit interactions based on phase change materials. *Adv Sci* 2018; **5**: 1800835.

29 Yang S, He M, Hong C, *et al.* Engineering electromagnetic field distribution and resonance quality factor using slotted quasi-bic metasurfaces. *Nano Lett* 2022; **22**: 8060–8067.

30 Hu S, Li P, Chen H, *et al.* Photonic meta-crystals. *Microstructures* 2025; **5**: 2025082.

31 Yang X, Wen E, Sievenpiper D. All-passive microwave-diode nonreciprocal metasurface. *Commun Phys* 2023; **6**: 333.

32 Yang W, Qin J, Long J, *et al.* A self-biased non-reciprocal magnetic metasurface for bidirectional phase modulation. *Nat*

Electron 2023; **6**: 225–234.

33 Tripathi A, Ugwu CF, Asadchy VS, *et al.* Nanoscale optical nonreciprocity with nonlinear metasurfaces. *Nat Commun* 2024; **15**: 5077.

34 Cotrufo M, Cordaro A, Sounas DL, *et al.* Passive bias-free non-reciprocal metasurfaces based on thermally nonlinear quasi-bound states in the continuum. *Nat Photon* 2024; **18**: 81–90.

35 Dong T, Li S, Manjappa M, *et al.* Nonlinear THz-nano metasurfaces. *Adv Funct Mater* 2021; **31**: 2100463.

36 Yuan J, Lu Z, Xu G, *et al.* Pump-wavelength selective all-optical terahertz metasurface with independent amplitude and frequency modulations. *Nano Lett* 2024; **24**: 15414–15420.

37 He W, Cheng X', Hu S, *et al.* Color coded metadevices toward programmed terahertz switching. *Light Sci Appl* 2024; **13**: 142.

38 Zhang J, Lou J, Wang Z, *et al.* Photon-induced ultrafast multitemporal programming of terahertz metadevices. *Adv Mater* 2025; **37**: 2410671.

39 Kumar A, Tan YJ, Navaratna N, *et al.* Slow light topological photonics with counter-propagating waves and its active control on a chip. *Nat Commun* 2024; **15**: 926.

40 Wen Y, Giorgianni F, Ilyakov I, *et al.* A universal route to efficient non-linear response via Thomson scattering in linear solids. *Natl Sci Rev* 2023; **10**: nwad136.

41 Wang C, Tan Y, Wen Y, *et al.* Nonperturbative nonlinear metasurfaces for efficient terahertz harmonic generation. *ACS Photon* 2024; **11**: 1236–1243.

42 Di Gaspare A, Song C, Schiattarella C, *et al.* Compact terahertz harmonic generation in the Reststrahlenband using a graphene-embedded metallic split ring resonator array. *Nat Commun* 2024; **15**: 2312.

43 Ruzicka BA, Werake LK, Samassekou H, *et al.* Ambipolar diffusion of photoexcited carriers in bulk GaAs. *Appl Phys Lett* 2010; **97**: 262119.

44 Wang S, Niu W, Fang YW. Nonlinear Hall effect in two-dimensional materials. *Microstructures* 2025; **5**: 2025060.

45 Lee K, Park J, Kang BJ, *et al.* Electrically controllable terahertz second-harmonic generation in GaAs. *Adv Opt Mater* 2020; **8**: 2000359.

46 Blotekjaer K. Transport equations for electrons in two-valley semiconductors. *IEEE Trans Electron Dev* 1970; **17**: 38–47.

47 Mayer A, Keilmann F. Far-infrared nonlinear optics. II. $\chi^{(3)}$ contributions from the dynamics of free carriers in semiconductors. *Phys Rev B* 1986; **33**: 6962–6968.

48 Khurgin J, Bykov AY, Zayats AV. Hot-electron dynamics in plasmonic nanostructures: Fundamentals, applications and overlooked aspects. *eLight* 2024; **4**: 15.

49 Hu S, He W, Tong M, *et al.* Dual-dimensional EIT manipulation for angle-multiplexed ultrafast terahertz switching. *ACS Photon* 2023; **10**: 2182–2191.

50 Lou J, Jiao Y, Yang R, *et al.* Calibration-free, high-precision, and robust terahertz ultrafast metasurfaces for monitoring gastric cancers. *Proc Natl Acad Sci USA* 2022; **119**: e2209218119.

51 Callan JP. Ultrafast dynamics and phase changes in solids excited by femtosecond laser pulses. Dissertation for Doctoral Degree. Cambridge: Harvard University, 2000.

52 Kuznetsov AV, Stanton CJ. Theory of coherent phonon oscillations in semiconductors. *Phys Rev Lett* 1994; **73**: 3243–3246.

53 Haug H, Koch SW. *Quantum Theory of the Optical and Electronic Properties of Semiconductors*. Singapore: World Scientific, 2009.

54 Su FH, Blanchard F, Sharma G, *et al.* Terahertz pulse induced intervalley scattering in photoexcited GaAs. *Opt Express* 2009; **17**: 9620.

55 Yang R, Zhang F, Li Z, *et al.* Controllable electromagnetically induced transparency in an electrically tunable terahertz hybrid metasurface. *Opt Laser Tech* 2023; **163**: 109380.

56 Fu S, Huang X, Gao G, *et al.* Unveiling high-mobility hot carriers in a two-dimensional conjugated coordination

polymer. *Nat Mater* 2025; **24**: 1457–1464.

57 Grady NK, Heyes JE, Chowdhury DR, *et al.* Terahertz metamaterials for linear polarization conversion and anomalous refraction. *Science* 2013; **340**: 1304–1307.

58 Song Q, Odeh M, Zúñiga-Pérez J, *et al.* Plasmonic topological metasurface by encircling an exceptional point. *Science* 2021; **373**: 1133–1137.

59 Wang C, Wen Y, Tan Y, *et al.* On-demand generation and control of giant terahertz nonlinearity with metasurfaces. *Laser Photon Rev* 2025; **19**: 2401224.

60 Wang S, Qin W, Guan T, *et al.* Flexible generation of structured terahertz fields via programmable exchange-biased spintronic emitters. *eLight* 2024; **4**: 11.